Journal of Materials Chemistry A

Accepted Manuscript

ROYAL SOCIETY OF CHEMISTRY

www.rsc.org/materialsA

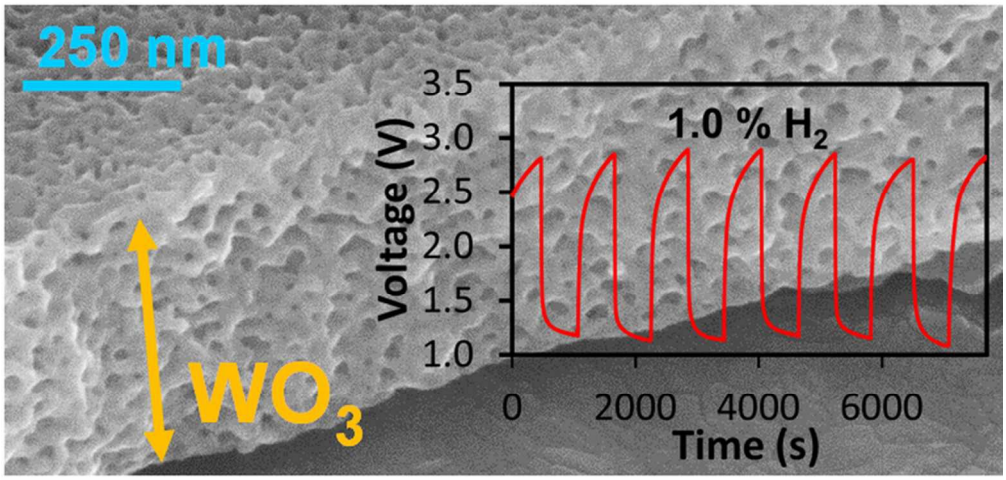

Reproducibility of the gas sensor made of 500 nm thick WO_3 nanoporous film upon exposure to hydrogen gas at 200 °C.
80x40mm (300 x 300 DPI)

Journal Name

RSCPublishing

ARTICLE

Anodized Nanoporous WO_3 Schottky Contact Structure for Hydrogen and Ethanol Sensing

Cite this: DOI: 10.1039/x0xx00000x

Rosmalini Ab. Kadir[a,*], Wei Zhang[a], Yichao Wang[a], Jian Zhen Ou[a], Wojtek Wlodarski[a], Anthony P. O'Mullane[b], Gary Bryant[c], Matthew Taylor[c], and Kourosh Kalantar-zadeh[a,*]

Received 00th January 2012,
Accepted 00th January 2012

DOI: 10.1039/x0xx00000x

www.rsc.org/

This paper reports the development of nanoporous tungsten trioxide (WO_3) Schottky diode-based gas sensors. The nanoporous WO_3 films were prepared by anodic oxidation of tungsten foil in ethylene glycol mixed with ammonium fluoride and a small amount of water. Anodization resulted in highly ordered WO_3 films with a large surface-to-volume ratio. Utilizing these nanoporous structures, Schottky diode-based gas sensors were developed by depositing a platinum (Pt) catalytic contact and tested towards hydrogen gas and ethanol vapour. Analysis of the current–voltage characteristics and dynamic responses of the sensors indicated that these devices exhibited a larger voltage shift in the presence of hydrogen gas compared to ethanol vapour at an optimum operating temperature of 200 °C. The gas sensing mechanism was discussed, associating the response to the intercalating H^+ species that are generated as the result of the hydrogen and ethanol molecules breakdowns onto Pt/WO_3 contact and their spill over into nanoporous WO_3.

Introduction

Tungsten trioxide (WO_3) is a *n*-type semiconductor with a band gap reported in the range of 2.6 to 3.3 eV, which has a wide range of applications due to its excellent electrical and optical properties.[1-4] Various WO_3 morphologies have been synthesized using different physical and chemical routes. Chemical routes including hydrothermal, solvothermal, anodization and thermal oxidation methods have shown to result in various morphologies including nanowires, nanorods, nanosheets, nanoparticles, and nanoplatlets as well as nanoporous films.[5-12] The aforementioned structures have been studied for diverse applications such as electrochromic smart windows, batteries, catalysts, electronic devices and solar cells.[5-7, 11-16] WO_3 is also one of the most interesting and most researched metal oxides for sensing gases such as hydrogen (H_2), hydrogen sulfide (H_2S), hydrocarbons, ethanol (C_2H_5OH), ammonia (NH_3), nitrogen oxide (NO_2, NO and N_2O) and carbon oxide (CO).[13-14, 17-20] Many of these investigations are focused on conductometric based gas sensors, and the application of WO_3 nanostructures in contact based systems, including Schottky diode-based sensors, have received rather limited attention.[21-22] The interaction of WO_3 with hydrogen atom containing molecules is generally the most efficient when it is of an intercalating nature. In this case, the intercalated H^+ ions are embedded into the crystal structure of WO_3 and the released electrons are transferred to the lowest-lying unoccupied energy levels of WO_3. Such an interaction changes the band structure of the WO_3 system and increases its conductivity, both of which can be used for sensing applications of the hydrogen atom containing molecules.[23]

The electron affinity of WO_3 is in the order of 3.2 to 4.0 eV.[24] As a result, a Schottky diode-based sensor can be developed by depositing a large work function noble metal such as platinum (Pt) (work function of 5.7 eV), gold (Au) (work function of 5.4 eV) and palladium (Pd) (work function of 5.6 eV) as the adjoining electrode.[25] In addition, these noble metals can act as excellent catalysts for enhancing the gas

reactions and augmenting the overall performance of the sensor.[26-27] The operating principles of the Schottky based sensors are primarily associated with the observation of the shifts in I–V curve caused by dissociation of the gas analyte on the catalytic metal surface which alters the Schottky barrier height at the metal-metal oxide interface.[28-30] This causes an effective change in the semiconductor work function, resulting in a voltage change across it. This consequently changes the current through the junction as well.

The gas sensing characteristics of the Schottky diode-based are greatly influenced by the morphology and porosity of the structures at the contacts interface, the contact metal and the semiconducting materials.[31] The reduction of the components' morphologies to nano dimensions can also alter the behavior of the systems.[32] Obviously, the alteration of surface energy, an increase in the surface to volume ratio, adjustments with relation to Debye length and stoichiometry of the semiconducting material are all important factors that affect the characteristics of the Schottky based sensors.[33-37] Additionally, the porosity of the semiconductor components enhances gas diffusion through the film and increases gas interaction and eventually adsorption of the gas molecules which can improve the sensor's performance.[38-39]

There are many reports regarding the development of nanoporous structures and thin films of metal oxides for improving the performance of gas sensors.[40-44] One of the most extensively investigated methods to fabricate highly porous metal oxides is anodization. Anodization generally occurs by applying a voltage across two electrodes that include one made of the base metal forming the porous metal oxide and the other a reference electrode in a suitable electrolyte. Anodization can potentially offer a simple and efficient process to obtain films with large surface area, tunable pores sizes and highly ordered morphologies.[45-48]

To the best of authors' knowledge, there is no report in the literature regarding the synthesis of WO_3 Schottky-based gas sensors *via* an anodization approach. Therefore, in this report, we demonstrate the performance of a WO_3 Schottky-based gas sensor prepared by anodization of W foil. The synthesis was performed in a mixed ethylene glycol-water solvent containing a small amount of NH_4F at room temperature. In this work, we studied and compared the performances of Schottky diode-based gas sensor towards hydrogen gas and ethanol vapour. The sensor performances such as voltage shift, response and recovery time have been investigated and discussed in detail.

Experimental

Synthesis of WO_3

W foil (99.9% purity) used in this work was purchased from Sigma Aldrich and cut into pieces of 1.0 cm × 1.5 cm. These substrates were cleaned with acetone in an ultrasonic bath, washed with isopropanol and deionized water then dried in a stream of nitrogen gas. After the clean-up, the substrates were anodized in an electrolyte of 50 mL ethylene glycol (98% anhydrous) mixed with 10% (wt) NH_4F (98% purity) (both from Sigma-Aldrich) and 2 vol.% of DI water. The anodization was carried out with a conventional two electrode configuration at room temperature,[49] where the anode was the W foil piece and the cathode was a platinum foil. Anodization at a voltage of 10 V for a duration of 15 minutes resulted in WO_3 films comprising of ~500 nm thick nanoporous structures. Upon the completion of the anodization experiment, samples were washed using DI water and dried in a nitrogen stream. The as-anodized samples were then annealed using a standard laboratory horizontal furnace at 500 °C for 1 h in air with a ramp-up and ramp-down rate of 2 °C min^{-1} which resulted in crystalline WO_3 films.

For fabricating the gas sensors, a Pt catalytic contact with a thickness of ~15 nm was deposited on top of the WO_3 nanoporous using a GATAN PECS™ (Precision Etching Coating System) thin film coater. The non-anodized side of the W substrates were used as the ohmic contact (Figure 1a).

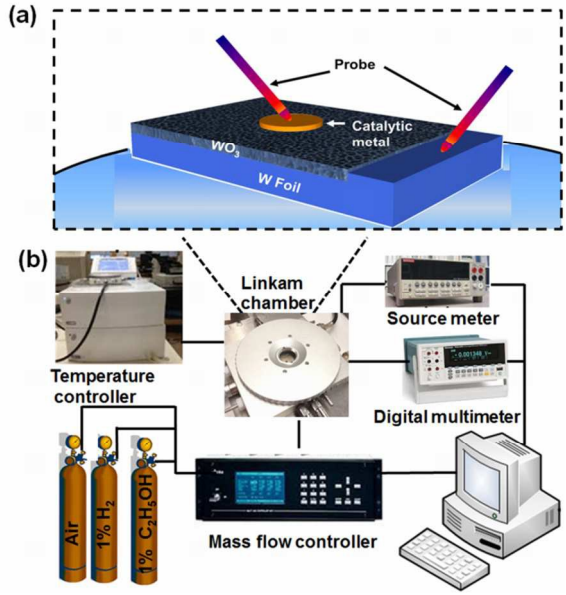

Figure 1. The schematic diagrams of (a) three-dimensional Schottky-based WO_3 sensor and (b) the gas sensing measurement set-up.

Structural Characterizations

The films morphologies were assessed using a scanning electron microscope (SEM - FEI Nova NanoSEM), while the chemical properties of the films were investigated by X-ray photoemission spectroscopy (XPS) using a Thermo K-alpha X-ray source (1486.7 eV) with pass energy of 50 eV. The crystallinity of the WO_3 films was characterized by a D8 Advance Bruker AXS X-ray diffractor with General Area Detector Diffraction System (GADDS) attachment fitted with a 50 μm spot size collimator, incorporating a High Star 2 dimensional detector and CuKα radiation (λ = 0.1542 nm) operating at 40 kV and 40 mA. Small angle XRD (SAXD) measurements were collected on a Bruker Microcalix

instrument, using 50 W CuKα radiation at a wavelength of 1.54 Å. Scattered light was detected using a Pilatus 100 k detector. Scattering and transmission measurements were made with 1 hour exposure time. Data analysis (normalization, primary beam masking, background subtraction) were carried out in fit-2D. No smoothing was used, and the fit results were not significantly affected by normalization. Raman spectroscopy was performed using a 785 nm laser at 0.9 mW power with a PerkinElmer Raman Station 400F.

Gas Sensing Measurements

During the measurements, the sensors were placed in a gas testing chamber connected to the T95 controller (both from Linkam Scientific Instruments), which was capable of controlling the temperature of the device *via* an external micro heater beneath the sensors. The operating system was accessed through Linksys 32 Software Package enabling the users to quickly enter experimental parameters such as temperature and heating rate. A thermocouple is connected to the stage for measuring the sensor surface temperatures online. Detail of the measurement set-up can be seen in the schematic diagram as presented in Figure 1b.

The electrical contact was formed by connecting the needle probes to the Pt electrodes of the sensors. The current–voltage (I–V) characteristics were measured using a Keithley 2600 current source meter. The gas sensor was supplied with a constant bias current (200 μA) in order to measure the dynamic response of the device when it was periodically exposed to ambient air and the analyte gas (hydrogen/ethanol) with the pulse sequence of 0.06%, 0.12%, 0.25%, 0.50% and 1%. The voltage change was recorded utilizing an Agilent 34410A digital multimeter. The concentration was accurately controlled using a computerized mass flow controller (MFC) multi-channel gas calibration system by changing the synthetic air to analyte gas ratio while maintaining a total constant flow rate of 200 SCCM (mL/min).

Results and Discussion

Morphology and Structural Properties

The SEM images of the annealed WO_3 films fabricated using an anodization voltage of 10 V for 15 minutes at room temperature are presented in Figure 2. From the top-view SEM image of the WO_3 layer of Figure 2(b, c), it is evident that a highly ordered self-organized three-dimensional (3D) nanoporous layer is formed on the entire surface. This porous layer consists of a very regular structure with pores encapsulated by interconnected walls. The pores have average dimensions in the order of 10 to 30 nm and a pore wall thickness ranging from 10 to 20 nm. The magnified cross sectional image of WO_3 (Figure. 2d) reveals a porous film with a thickness of ~500 nm. It has been reported that, the sensing properties can be enhanced as the thickness of semiconductor metal oxide film decreased.[41, 50] This thickness was chosen as a thickness below 500 nm could not be implemented due to the short circuit while forming the Schottky contacts.

In order to examine the composition of the porous WO_3 layers, XPS analysis was carried out. Figure 3a shows the XPS spectra obtained from wide survey scan presenting peaks of W, O, N and C. The presence of carbon and nitrogen on the surface is attributed to atmospheric contamination. Figure 3b shows the high resolution core level W 4f spectra of WO_3 films. The binding energies of 35.4 and 37.9 correspond to W $4f_{7/2}$ and W $4f_{5/2}$, respectively,[51] indicating that the formed films consist essentially of WO_3.

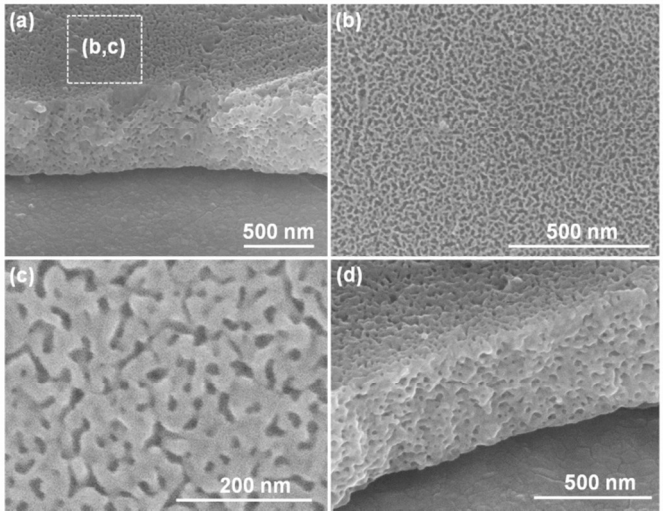

Figure 2. SEM images of annealed WO_3 (a) cross sectional view (b) top view (c) a magnified image of the interface in (b) and (d) a magnified image of cross sectional view

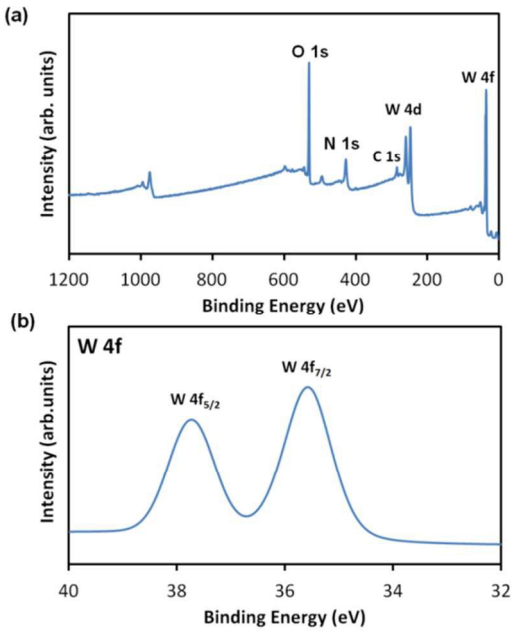

Figure 3. (a) The XPS survey scan of nanoporous WO_3 film and (b) XPS spectrum of W 4f peaks of the nanoporous WO_3 film.

Figure 4a shows the X-ray diffraction (XRD) patterns of the WO_3 films before and after annealing. According to the XRD patterns in Figure 4a, the as-anodized nanoporous WO_3 film appears to be amorphous as only the tungsten peaks exist (ICDD 04-0806).[11, 52] The strongest diffraction peaks appear at 2θ = 23.2, 24.1, 29.5, 33.9, 42.0, 49.5 and 55.5° for the annealed sample. The peaks clearly show the crystalline signature of the orthorhombic phase (ICDD 20-1324) of WO_3, which is consistent with previous reports.[11, 52]

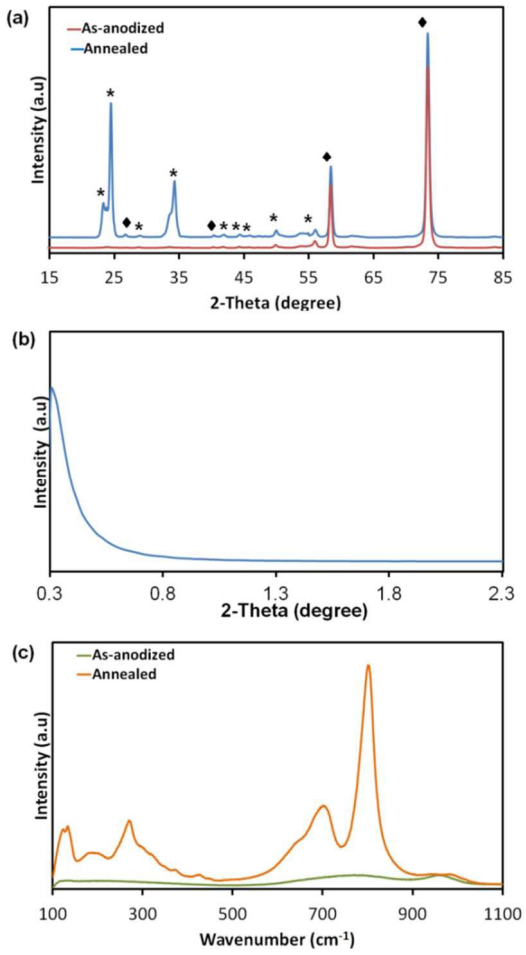

Figure 4. (a) The XRD patterns of nanoporous WO_3 film: as-anodized and after annealing in air for 1 hour at 450 °C. The orthorhombic phase (ICDD 20-1324) is denoted by * while the as anodized film is amorphous as only the tungsten peaks exist (ICDD 04-0806) (denoted by ♦), (b) SAXD diffraction pattern of the annealed WO_3 film and (c) the Raman spectra of the as-anodized and annealed nanoporous WO_3 films.

The pore dimensions were obtained using SAXD as suggested in the report by Li *et al*.[53] The SAXD pattern (Figure 4b) of WO_3 film shows a single diffraction peak at low 2θ. The approximate pore dimension is determined to be about 25 nm, which falls within the meso domain range (the BET surface area analysis is presented in the Supplementary Information).[54] The XRD result was further verified by the Raman spectra presented in Figure 4c. The as-anodized WO_3 film exhibited two weak and broad Raman bands centered at 770 and 960 cm^{-1}, respectively. After annealing, new peaks appeared at 704 and 804 cm^{-1} as well as at 134 and 272 cm^{-1}, which are indicative of the O–WO_3 orthorhombic phase of the films.[11, 52] This pattern can be assigned to either the monoclinic or orthorhombic phase, as it has been reported that the monoclinic phase of WO_3 has a very similar Raman pattern to that of the orthorhombic phase.[11] However, the orthorhombic phase is more likely as evidenced by the XRD analysis.

Gas Sensing Performance

The I–V characteristics were obtained in the presence of air and alternately with 1% hydrogen gas (Figure 5a) or ethanol vapour (Figure 5b), respectively at temperatures ranging from 50 °C to 300 °C. As the operating temperature increased, the relative change in the I–V characteristics was observed with a very good non-linear curve which is typical of the electrical properties of these structures.[55-56] The I–V curve obtained showed a comparatively low current at 50 °C since the charge carriers have insufficient energy to overcome the barrier height energy. However, as the temperature increased, we observed a larger current flow as a result of augmentation in the carrier's energy. The increase in current can also be due to an increase in the number of electron-hole pairs as a result of higher thermal energy.[56-58] Furthermore, the changes in current were larger upon exposures to hydrogen gas and ethanol vapour. This is because hydrogen ions which diffuse and intercalate with WO_3 decrease the Schottky barrier height (SBH),[28] which dopes the material and also the formation of dipoles near the junction. The joint effect can result in more carriers with sufficient energies to flow over the lowered energy barrier *via* the thermionic emission mechanism.[59-60] The mechanism of gas sensing will be discussed in detail in the following section.

As can be seen from Figure 5, the largest lateral voltage shift of the sensor towards hydrogen gas was observed at 200 °C, while for the exposure towards ethanol vapour, the largest voltage shift occurred at 300 °C. It is suggested that ethanol vapour dissociates by catalytic metals at higher temperatures as compared to hydrogen. It has been reported that dissociation of ethanol begins at a temperature of ~55 °C and the process were maximized at 300 °C.[61] The optimum operating temperature for the maximum voltage shift of hydrogen being lower compared to ethanol agrees well with the other previously reported Schottky-based sensors.[41-42, 62] The voltage shift of each sensor is attributed to the reduction of the SBH, which can be calculated using the thermionic emission equation. The dependence of forward current on the applied voltage of a Schottky diode is given by the expression:[56]

$$I_F = I_s\left\{exp\left(\frac{qV_F}{kT}\right) - 1\right\} \quad (1)$$

where I_s, q, V_F, T and k are the saturation current in ampere, the charge of one electron in Coulombs, the forward applied voltage in volts, the absolute temperature in Kelvin and the Boltzmann's constant, respectively. The I_s is defined by:

$$I_s = AA^{**}T^2exp\left(-\frac{q\Phi_B}{kT}\right) \quad (2)$$

in which A is the diode area in m^2, A^{**} is the Richardson constant and Φ_B is the Schottky barrier height in eV. Using equation (2), the SBH can be determined. The SBH change in the presence of hydrogen and in the presence of ethanol at different temperatures were calculated and shown in Table 1.

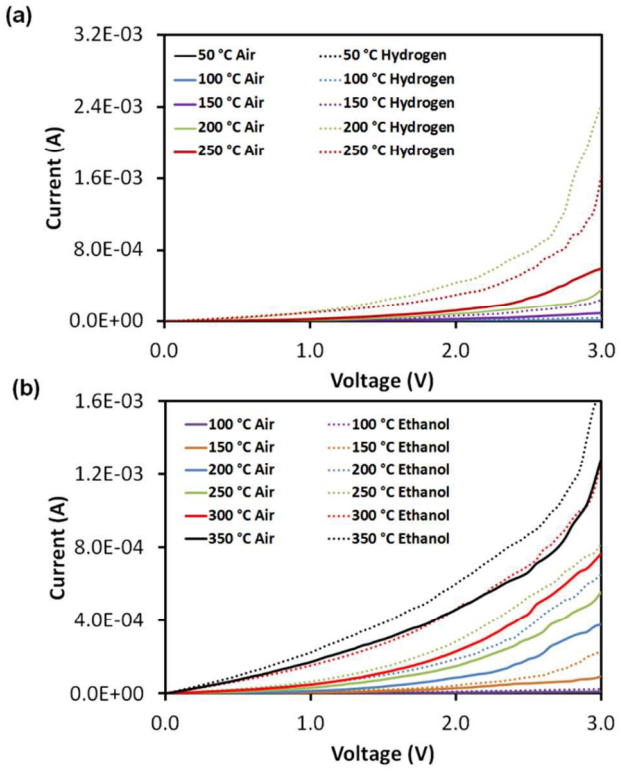

Figure 5. (a) The forward IV characteristics of the nanoporous WO_3 gas sensor upon exposure to (a) hydrogen gas and (b) ethanol vapour.

As the largest lateral voltage shifts upon exposure to hydrogen and ethanol were observed at 200 and 300 °C, respectively, the dynamic responses of the sensor were investigated at these temperatures. The dynamic responses of the sensor with a constant bias current of 200 µA towards different concentrations of hydrogen gas and ethanol vapour, in an air background, are shown in Figure 6a and b respectively. The device demonstrated a very good response to hydrogen and ethanol at its respective optimum temperature, where the sensor's output returns to the baseline after recovery.

The stability of the sensor was investigated by repeatedly switching from air to 1 % hydrogen over a few cycles and presented in Figure 7. The sensor was found to have stable response and recovery characteristics, indicating that high repeatability and stability were achieved. The measurements were all conducted in non humid environment. It is believed that humidity will certainly deteriorate the response of the device as reported previously.[42, 63]

Table 1 Barrier height change at different temperatures.

Temperature (°C)	Barrier height change (eV)	
	$\Delta\Phi_{B(H_2)}$	$\Delta\Phi_{B(Eth)}$
50	0.029	0.011
100	0.039	0.018
150	0.047	0.022
200	0.065	0.028
250	0.035	0.032
300	-	0.041
350	-	0.033

The voltage shift in the presence of both hydrogen gas and ethanol vapour *vs* their different concentrations are presented in Figure 8. Voltage shifts of 0.8, 1.0, 1.2, 1.4 and 1.6 V were measured for 0.06, 0.125, 0.25, 0.5 and 1 % hydrogen gas, respectively. However, the same set of ethanol vapour concentration resulted in smaller voltage shifts which were 0.4, 0.5, 0.6, 0.7 and 0.8 V, respectively, as discussed previously. As the concentration of hydrogen gas or ethanol vapour increases, more hydrogen molecules will be adsorbed on the Pt catalytic surface and converted to H^+ ions. Consequently, a lower barrier height was observed resulting higher voltage shift. Additionally, it can be clearly seen that the sensor is more sensitive to hydrogen as compared to ethanol.

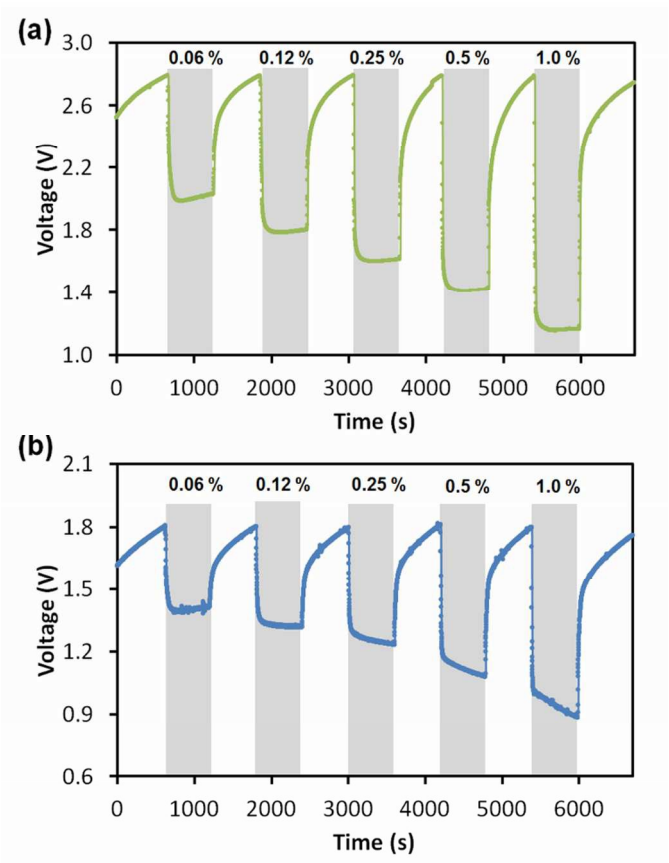

Figure 6. (a) The dynamic response of nanoporous WO_3 gas sensors measured with different concentrations of (a) H2 gas at 200 °C and (b) ethanol vapour at 300 °C with a constant bias current of 200 µA

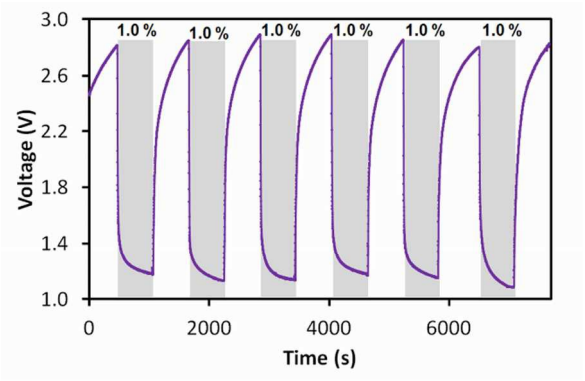

Figure 7. Reproducibility of the sensor upon exposure to hydrogen gas at 200 °C for 6 cycles.

The response factor (RF) in percentage is defined as the ratio of the voltage shift over the base voltage in air (V_{air}) and can be described as follows:

$$RF = \frac{V_{air} - V_{gas}}{V_{air}} \times 100\% \quad (3)$$

in which V_{gas} is the voltage when the device is exposed to gas. The gas sensor response factors were calculated as 27.5%, 35.3%, 42.1%, 49.3% and 58.2% for the aforementioned hydrogen gas concentrations, while the response factors were 22.2%, 25.6%, 30.6%, 37.8% and 43.9 % for the ethanol vapour with the same set of concentrations.

We further evaluated the performance of the WO_3 gas sensor in terms of the response and recovery time. The response time is defined as the time required for 90% of the total voltage change and the recovery time is the time taken for 90% recovery of the total voltage change. Response and recovery times were obtained for the nanoporous WO_3 Schottky diode sensor when exposed alternately to synthetic air with a hydrogen or ethanol balance concentration in the order of 0.06 - 1% and the data is shown in Table 2. The sensor's recovery time is longer than the response time. The same trend of response and recovery time for other nanoporous metal oxide gas sensors have been reported where the recovery time is generally longer than the response time upon exposure to a varies of analyte.[41, 64]

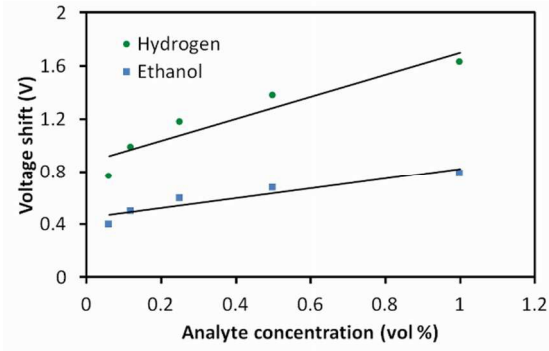

Figure 8. Voltage shifts of nanoporous WO_3 gas sensors at different concentrations of target gas.

As the concentration of gas analyte increases, a faster response is demonstrated. Conversely, the recovery time increases as the gas analyte concentration increases. It is suggested that, at higher concentrations of the target gas, a larger number of target gas molecules dissociate on the catalytic metal and adsorb inside the porous film.[65] As a result, a faster response is observed compared to response of the target gas at lower concentration. However, purging the target gas out from the nanoporous films takes a longer time as the concentration of the target gas in the films results in a larger stoichiometry changes within the films, which require longer recovery times to return to its initial condition.

Table 2 Response and recovery time of the sensor at different analyte concentrations.

Analyte concentration (vol %)	Hydrogen		Ethanol	
	Response time (s)	Recovery time (s)	Response time (s)	Recovery time (s)
0.06	43	108	55	128
0.12	38	111	42	139
0.25	29	124	32	153
0.5	23	151	27	172
1.0	20	180	25	185

A shorter response time is observed upon hydrogen exposure in comparison with the response to ethanol. Hydrogen gas dissociates directly to produce hydrogen ions, while ethanol vapour needs an additional dehydrogenation step where ethanol dissociates into ethoxides and acetaldehyde before generating the hydrogen ions.[66-67] Thus, the device demonstrated a longer response time upon exposure to ethanol vapour.

The sensing mechanism of the nanoporous WO_3 gas sensor is explained as follows:

Dissociative chemisorption of molecular hydrogen onto Pt, forming hydrogen ions (H^+) and electrons charge (e^-) is described by [68]:

$$H_2(g) \rightarrow 2H^+ + 2e^- \quad (4)$$

Similarly, on the catalyst surface, ethanol molecules start to dissociate into ethoxides and further oxidize into acetaldehyde as in equation (5) and (6) when the temperature increases. [69]

$$C_2H_5OH(g) \rightarrow CH_3CH_2O + H(ads) \quad (5)$$

$$C_2H_5O(a) \rightarrow CH_3CHO(g) + H(ads) \quad (6)$$

in which (g) and (ads) stand for the gaseous and adsorbed species, respectively. The H atoms produced from equation (5) and (6) are transformed into H^+ ions with the liberation of an electron e^- , resulting in adsorbed H^+.

The accumulated H^+ ions from equation (4) to (6) diffuse over the catalytic metal and intercalate with the WO_3 pore wall that can be described according to the following formula[5]:

$$WO_3 + xH^+ + xe^- \leftrightharpoons H_xWO_3 \quad (7)$$

The released electrons in equation (7) reduce the width of the depletion region in the oxide film, which decreases the resistance of the film and also the barrier height that corresponds to the voltage shift for the gas sensor.[68]

As the system is maintained at an elevated temperature, it is also possible that H_xWO_3 breaks down into reduced WO_3 producing H_2O vapour.[23]

$$2H_xWO_3 \leftrightharpoons xH_2O + 2WO_{3-x/2} \quad (8)$$

Upon exposing the sensors back to air (oxygen rich environment) the reduced oxide is restored to form WO_3 *via*:

$$WO_{3-x/2} + (x/4)O_2 \leftrightharpoons WO_3 \quad (9)$$

which allows the repeatability of the gas sensor.

For comparison with our work, responses of previously reported nanostructured WO_3 Schottky-based hydrogen gas sensors are summarized in Table 3. It is observed that our nanoporous Schottky-based gas sensor has the highest voltage shift at a relatively low operating temperature as compared to other works. The superior performance of our sensors is ascribed to the high porosity of WO_3 films, forming the sensing layer.

Table 3. Voltage shift of WO_3 Schottky-based gas sensors towards exposure to 1% hydrogen gas: comparison of previous reports with this work

Fabrication technique (morphology)	Optimum operating temperature (°C)	Voltage shift (V)	Refs.
RF sputtering (thin films)	150	0.03	22
RF sputtering (nanoplatlets)	300	1.14	70
RF sputtering (thin films)	530	0.08	71
RF sputtering (thin films)	150	0.40	65
Anodization (nanoporous)	200	1.67	This work

Conclusions

In this work, we successfully synthesized highly ordered nanoporous WO_3 films via the electrochemical anodization of W. Pt was deposited as a Schottky forming contact, which also provided catalytic properties for sensing hydrogen gas and ethanol vapor. The structural properties of WO_3 films were investigated using SEM, XRD, XPS and Raman spectroscopy demonstrating the existence of an orthorhombic crystal phase made of pores in the order of 10 to 30 nm in dimensions. The Pt/WO_3 Schottky-based gas sensor was tested towards hydrogen and ethanol molecules in gaseous environments. The porosity of the WO_3 structure resulted in a high surface-to-volume ratio film that facilitated the intercalating adsorption/desorption of gas molecules. Gas sensing measurements for the device exhibited the best performance towards hydrogen providing a voltage shift of 1.67 V for 1% hydrogen, when the device was biased at a current of 200 μA and was operated at 200 °C. The WO_3 nanoporous Schottky gas sensor also exhibited good reproducibility and repeatable responses with a stable baseline.

Acknowledgements

The authors acknowledge the facilities, and the scientific and technical assistance, of the Australian Microscopy & Microanalysis Research Facility at the RMIT Microscopy & Microanalysis Facility (RMMF), at RMIT University.

Notes and references

[a] School of Electrical and Computer Engineering, RMIT University, Melbourne, Victoria 3001, Australia

[b] School of Chemistry, Physics and Mechanical Engineering, Queensland University of Technology, Brisbane, Queensland 4001, Australia

[c] Centre for Molecular and Nanoscale Physics, School of Applied Sciences, RMIT University, Melbourne, Victoria 3001, Australia

1. Zheng, H.; Ou, J. Z.; Strano, M. S.; Kaner, R. B.; Mitchell, A.; Kalantar-zadeh, K., *Adv. Funct. Mater.,* 2011, **21**, 2175-2196.
2. Deb, S. K., *Sol. Energ. Mat. Sol. C,* 2008, **92**, 245-258.
3. Gillet, M.; Aguir, K.; Lemire, C.; Gillet, E.; Schierbaum, K., *Thin Solid Films,* 2004, **467**, 239-246.
4. Watanabe, H.; Fujikata, K.; Oaki, Y.; Imai, H., *Chem. Commun.,* 2013, **49**, 8477-8479.
5. Ou, J. Z.; Balendhran, S.; Field, M. R.; McCulloch, D. G.; Zoolfakar, A. S.; Rani, R. A.; Zhuiykov, S.; O'Mullane, A. P.; Kalantar-zadeh, K., *Nanoscale,* 2012, **4**, 5980-5988.
6. Sadek, A. Z., et al., *Langmuir,* **2009**, *25*, 9545-9551.
7. Cao, B.; Chen, J.; Tang, X.; Zhou, W., *J. Mater. Chem.,* 2009, **19**, 2323-2327.
8. Gu, Z.; Zhai, T.; Gao, B.; Sheng, X.; Wang, Y.; Fu, H.; Ma, Y.; Yao, J., *J. Phys. Chem., B,* 2006, **110**, 23829-23836.
9. Choi, H. G.; Jung, Y. H.; Kim, D. K., *J. Am. Ceram. Soc.,* 2005, **88**, 1684-1686.
10. Zhang, J.; Tu, J.-p.; Xia, X.-h.; Wang, X.-l.; Gu, C.-d., *J. Mater. Chem.,* 2011, **21**, 5492-5498.
11. Ou, J. Z.; Rani, R. A.; Balendhran, S.; Zoolfakar, A. S.; Field, M. R.; Zhuiykov, S.; O'Mullane, A. P.; Kalantar-zadeh, K., *Electrochem. Commun.,* 2013, **27**, 128-132.
12. Zeng, J.; Hu, M.; Wang, W.; Chen, H.; Qin, Y., *Sens. Actuators B,* 2012, **161**, 447-452.
13. Ou, J. Z.; Ahmad, M. Z.; Latham, K.; Kalantar-zadeh, K.; Sberveglieri, G.; Wlodarski, W., *Procedia Engineering,* 2011, **25**, 247-251
14. Rout, C. S.; Ganesh, K.; Govindaraj, A.; Rao, C. N. R., *Appl. Phys. A-Mater.,* 2006, **85**, 241-246.
15. Xue, X.-Y.; He, B.; Yuan, S.; Xing, L.-L.; Chen, Z.-H.; Ma, C.-H., *Nanotechnology,* 2011, **22**, 395702
16. Zheng, H.; Tachibana, Y.; Kalantar-zadeh, K., *Langmuir,* 2010, **26**, 19148-19152.
17. Ippolito, S. J.; Kandasamy, S.; Kalantar-zadeh, K.; Wlodarski, W., *Sens. Actuators B,* 2005, **108**, 154-158.
18. Ahsan, M.; Ahmad, M. Z.; Tesfamichael, T.; Bell, J.; Wlodarski, W.; Motta, N., *Sens. Actuators B,* 2012, **173**, 789-796.
19. Ahmad, M. Z.; Sadek, A. Z.; Ou, J. Z.; Yaacob, M. H.; Latham, K.; Wlodarski, W., *Mater. Chem. Phys.,* 2013, **141**, 912-919.

20. Siciliano, T.; Tepore, A.; Micocci, G.; Serra, A.; Manno, D.; Filippo, E., *Sens. Actuators B,* 2008, **133**, 321-326.
21. Shafiei, M.; Sadek, A. Z.; Yu, J.; Latham, K.; Breedon, M.; McCulloch, D.; Kalantar-zadeh, K.; Wlodarski, W., *Sens. Lett.,* 2011, **9**, 11-15.
22. Liu, Y.; Yu, J.; Cai, F. X.; Tang, W. M.; Lai, P. T., Electron Devices and Solid-State Circuits (EDSSC), 2013 IEEE International Conference of, 2013; pp 1-2.
23. Yaacob, M. H.; Breedon, M.; Kalantar-zadeh, K.; Wlodarski, W., *Sens. Actuators B,* 2009, **137**, 115-120.
24. Walter, C. W.; Hertzler, C. F.; Devynck, P.; Smith, G. P.; Peterson, J. R., P *J. Chem. Phys.,* 1991, **95**, 824-827.
25. Skriver, H. L.; Rosengaard, N. M., *Phys. Rev. B,* 1992, **46**, 7157-7168.
26. Haridas, D.; Sreenivas, K.; Gupta, V., *Sens. Actuators B,* 2008, **133**, 270-275.
27. Mizsei, J.; Sipilä, P.; Lantto, V., *Sens. Actuators B,* 1998, **47**, 139-144.
28. Lundström, I.; Shivaraman, S.; Svensson, C.; Lundkvist, L., *Appl. Phys. Lett.,* 1975, **26**, 55-57.
29. Yamamoto, N.; Tonomura, S.; Matsuoka, T.; Tsubomura, H., *Surf. Sci.,* 1980, **92**, 400-406.
30. Lundstrom, K. I.; Shivaraman, M. S.; Svensson, C. M., *J. Appl. Phys.,* 1975, **46**, 3876-3881.
31. Bourenane, K.; Keffous, A.; Nezzal, G.; Bourenane, A.; Boukennous, Y.; Boukezzata, A., *Sens. Actuators B,* 2008, **129**, 612-620.
32. Wang, C.; Yin, L.; Zhang, L.; Xiang, D.; Gao, R., *Sensors,* **2010**, *10*, 2088-2106.
33. Yu, J.; Ippolito, S. J.; Wlodarski, W.; Strano, M.; Kalantar-zadeh, K., *Nanotechnology,* 2010, **21**, 265502
34. Sun, Y.-F.; Liu, S.-B.; Meng, F.-L.; Liu, J.-Y.; Jin, Z.; Kong, L.-T.; Liu, J.-H., *Sensors,* 2012, **12**, 2610-2631.
35. Wei, T.-Y.; Yeh, P.-H.; Lu, S.-Y.; Lin-Wang, Z., *J. Am. Chem. Soc.,* 2009, **131**, 17690-17695.
36. Schierbaum, K. D.; Kirner, U. K.; Geiger, J. F.; Göpel, W., *Sens. Actuators B,* 1991, **4**, 87-94.
37. Shimizu, Y.; Egashira, M., *MRS Bulletin,* 1999, **24**, 18-24.
38. Wagner, T.; Haffer, S.; Weinberger, C.; Klaus, D.; Tiemann, M., *Chem. Soc. Rev.,* 2013, **42**, 4036-4053.
39. Hyodo, T.; Shimizu, Y.; Egashira, M., *Electrochemistry,* 2003, **71**, 387-393.
40. Hossein-Babaei, F.; Abbaszadeh, S.; Esfahani, M. S., *IEEE Sens. J.,* 2009, **9**, 237-243.
41. Rani, R. A.; Zoolfakar, A. S.; Ou, J. Z.; Field, M. R.; Austin, M.; Kalantar-zadeh, K., *Sens. Actuators B,* 2013, **176**, 149-156.
42. Kadir, R. A.; Rani, R. A.; Zoolfakar, A. S.; Ou, J. Z.; Shafiei, M.; Wlodarski, W.; Kalantar-zadeh, K., *Sens. Actuators B,* 2014, **202**, 74-82.
43. Salehi, A.; Nikfarjam, A.; Kalantari, D. J., *Sens. Actuators B,* 2006, **113**, 419-427.
44. Salehi, A.; Kalantari, D. J., *Sens. Actuators B,* 2007, **122**, 69-74.
45. Macak, J. M.; Tsuchiya, H.; Ghicov, A.; Yasuda, K.; Hahn, R.; Bauer, S.; Schmuki, P., *Curr. Opin. Solid St. M,.* 2007, **11**, 3-18.
46. Masuda, H.; Hasegwa, F.; Ono, S., *J. Electrochem. Soc.,* 1997, **144**, L127-L130.
47. Prakasam, H. E.; Shankar, K.; Paulose, M.; Varghese, O. K.; Grimes, C. A., *J. Phys. Chem. C,* 2007, **111**, 7235-7241.
48. Pandey, B.; Thapa, P. S.; Higgins, D. A.; Ito, T., *Langmuir,* 2012, **28**, 13705-13711.
49. Zheng, H.; Sadek, A. Z.; Latham, K.; Kalantar-Zadeh, K., *Electrochem. Commun.,* 2009, **11**, 768-771.
50. Chang, J. F.; Kuo, H. H.; Leu, I. C.; Hon, M. H., *Sens. Actuators B,* 2002, **84**, 258-264.
51. Ou, J. Z.; Yaacob, M. H.; Breedon, M.; Zheng, H. D.; Campbell, J. L.; Latham, K.; Plessis, J. d.; Wlodarski, W.; Kalantar-zadeh, K., *Phys. Chem. Chem. Phys.,* 2011, **13**, 7330-7339.
52. Kalantar-zadeh, K.; Vijayaraghavan, A.; Ham, M.-H.; Zheng, H.; Breedon, M.; Strano, M. S., *Chem. Mater.,* 2010, **22**, 5660-5666.
53. Li, J.; Liu, X.; Han, Q.; Yao, X.; Wang, X., *J. Mater. Chem. A,* 2013, **1**, 1246-1253.
54. Soler-Illia, G. J. d. A. A.; Sanchez, C.; Lebeau, B.; Patarin, J., *Chem. Rev.,* 2002, **102**, 4093-4138.
55. Chiu, S.-Y.; Huang, H.-W.; Huang, T.-H.; Liang, K.-C.; Liu, K.-P.; Tsai, J.-H.; Lour, W.-S., *Sens. Actuators B,* 2009, **138**, 422-427.
56. Sze, S. M.; Ng, K. K., *Physics of Semiconductor Devices*, 3rd ed.; Hoboken, NJ, USA: John Wiley & Sons, Inc, 2007.
57. Xu, J. P.; Lai, P. T.; Zhong, D. G.; Chan, C. L., *IEEE Electron Device L.,* 2003, **24**, 13-15.
58. Shafiei, M.; Yu, J.; Arsat, R.; Kalantar-zadeh, K.; Comini, E.; Ferroni, M.; Sberveglieri, G.; Wlodarski, W., *Sens. Actuators B,* **2010**, **146**, 507-512.
59. Pitcher, S.; Thiele, J. A.; Ren, H.; Vetelino, J. F., *Sens. Actuators B,* 2003, **93**, 454-462.
60. Tsai, T.-H.; Huang, J.-R.; Lin, K.-W.; Hsu, W.-C.; Chen, H.-I.; Liu, W.-C., *Sens. Actuators B,* 2008, **129**, 292-302.
61. Alonso, C. G.; Furtado, A. C.; Cantao, M. P.; dos Santos, O. A. A.; Fernandes-Machado, N. R. C., *Int. J. Chem. React. Eng.,* 2009, **7**, Art.No.A42
62. Xing, L.-L.; He, B.; Chen, Z.-H.; Xue, X.-Y., *Solid State Sci.,* 2013, **15**, 42-46.
63. Talazac, L.; Barbarin, F.; Varenne, C.; Mazet, L.; Pellier, S.; Soulier, C., *Sens. Actuators B* 2002, **83**, 149-159.
64. Yamamoto, G.; Yamashita, T.; Matsuo, K.; Hyodo, T.; Shimizu, Y., *Sens. Actuators B,* 2013, **183**, 253-264.
65. Liu, Y.; Yu, J.; Lai, P. T., *Int. J. Hydrogen Energ.,* 2014, **39**, 10313-10319.
66. Ivanovskaya, M.; Kotsikau, D.; Faglia, G.; Nelli, P.; Irkaev, S., *Sens. Actuators B,* 2003, **93**, 422-430.
67. Han, G.; Lu, Q.; Liu, G.; Ye, X.; Lin, S.; Song, Y.; Liu, B.; Yang, X.; Li, G., *J. Mater. Sci-Mater., El* 2012, **23**, 1616-1620.
68. Hübert, T.; Boon-Brett, L.; Black, G.; Banach, U., *Sens. Actuators B,* 2011, **157**, 329-352.
69. Sexton, B. A.; Rendulic, K. D.; Huges, A. E., *Surf. Sci.,* 1982, **121**, 181-198.
70. Shafiei, M.; Yu, J.; Sadek, A. Z.; Nunzio, M.; Kalantar-zadeh, K.; Wlodarski, W. 4th International Conference on Nanostructures (ICNS4), 2012; pp 889-891.
71. Kandasamy, S.; Trinchi, A.; Wlodarski, W.; Comini, E.; Sberveglieri, G., *Sens. Actuators B,* 2005, **111–112**, 111-116.

